Volume 26
Number 21
7 June 2024
Pages 2739–2844

CrystEngComm

rsc.li/crystengcomm

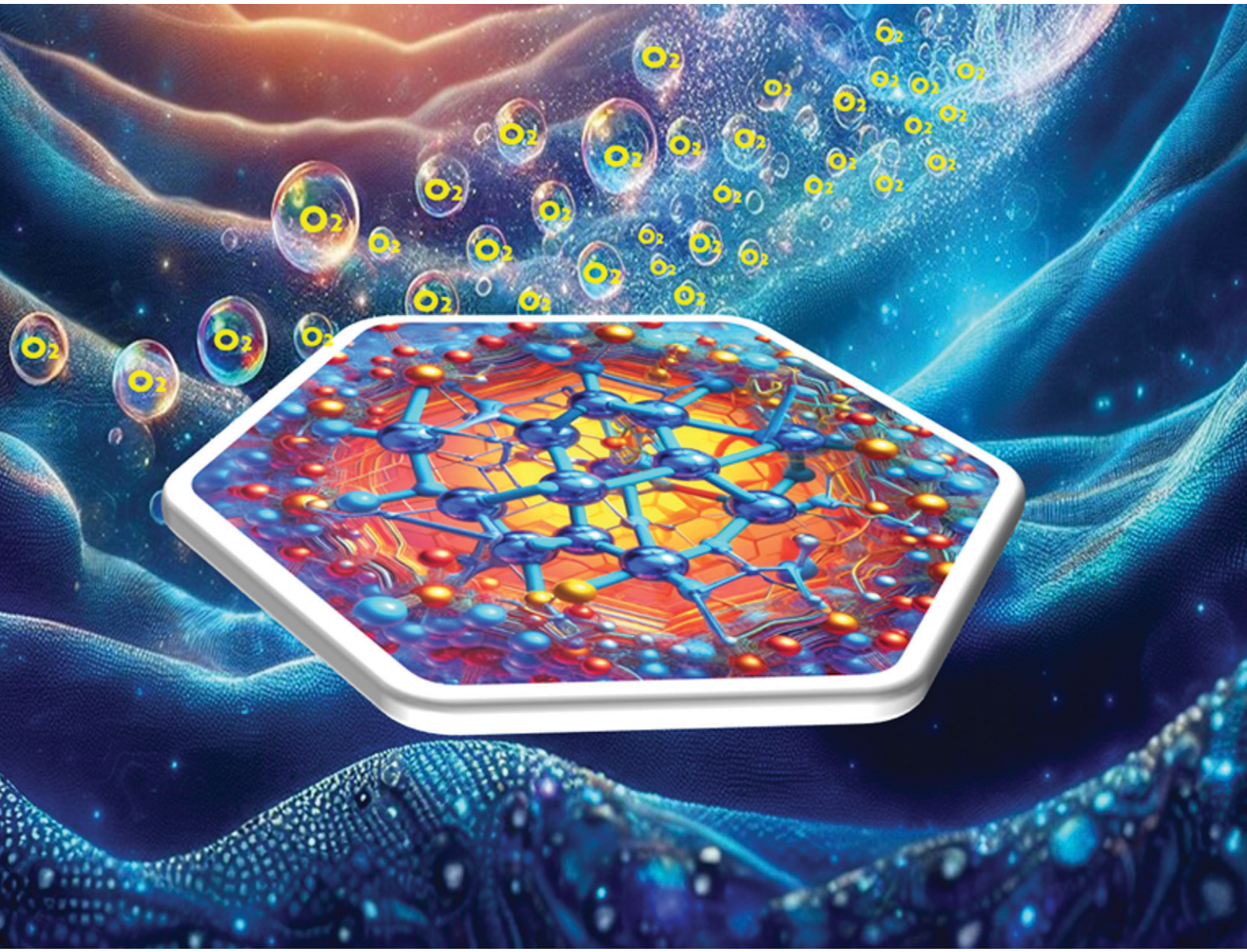

ISSN 1466-8033

ROYAL SOCIETY OF CHEMISTRY

PAPER

Anup Paul *et al.*

Catalyzing towards clean energy: tuning the oxygen evolution reaction by amide-functionalized Co(II) and Ni(II) pristine coordination polymers

CrystEngComm

ROYAL SOCIETY OF CHEMISTRY

PAPER

View Article Online
View Journal | View Issue

Cite this: *CrystEngComm*, 2024, **26**, 2755

Catalyzing towards clean energy: tuning the oxygen evolution reaction by amide-functionalized Co(II) and Ni(II) pristine coordination polymers†

Anup Paul, *[a] Filipe Gusmão, [b] Abdallah G. Mahmoud, [ac] Susanta Hazra, [a] Lazar Rakočević, [d] Biljana Šljukić, *[b] Rais Ahmad Khan, [e] M. Fátima C. Guedes da Silva [af] and Armando J. L. Pombeiro *[a]

Received 27th February 2024,
Accepted 25th April 2024

DOI: 10.1039/d4ce00179f

rsc.li/crystengcomm

We present the synthesis and characterization of two monometallic coordination polymers, $[Co(L)_2(H_2O)_2]_n$ (**Co-CP**) and $[Ni(L)_2(H_2O)_2]_n$ (**Ni-CP**), alongside a heterobimetallic counterpart, **CoNi-CP**, derived from an amide-based multifunctional pro-ligand 4-(pyrimidin-5-ylcarbamoyl)benzoic acid (HL), and discussed their electrocatalytic activity in the oxygen evolution reaction (OER). The CPs were characterized using various techniques, including elemental analysis, IR spectroscopy, X-ray diffraction, and thermal and powder XRD analyses. The low-cost amide-functionalized transition metal pristine coordination polymers **Co-CP** and **Ni-CP** were demonstrated to catalyze the OER in alkaline media, surpassing the benchmark IrO_2 electrocatalyst performance. The heterometallic coordination polymer (**CoNi-CP**) displayed a lower Tafel slope value (and thus, faster kinetics) and higher long-term durability compared to its monometallic counterparts, **Co-CP** and **Ni-CP**. The results obtained show a pristine transition metal heterobimetallic coordination polymer as a low-cost electrocatalyst of great promise and high performance for OER catalysis in alkaline media.

Introduction

Fuel cells, metal-air batteries and water-splitting devices stand as bases in renewable energy, offering sustainable and eco-friendly solutions. Central to their efficiency, especially in water electrolysis and rechargeable metal-air batteries, lies the oxygen evolution reaction (OER).[1–4] However, the slow rate of reactions of the OER presents a formidable task, hindering the broader deployment of these technologies. While benchmark catalysts like RuO_2 and IrO_2 exist, their cost, availability, and stability issues in various electrolytes limit their practicality.[5] Hence, the quest for cost-effective, efficient OER catalysts is paramount.

In response to this challenge, considerable efforts have been channeled into developing transition metal-based electrocatalysts with enhanced OER properties.[6,7] Coordination polymers (CPs) and metal–organic frameworks (MOFs) have risen as notable structures in coordination chemistry, possessing tunable pore structures, large surface areas, and catalytically active metal centers.[8–11] By incorporating organic linkers and metals within these frameworks, we harness their dual role, providing redox-active centers and proton transfer pathways vital for OER catalysis.[8–11]

[a] *Centro de Química Estrutural, Institute of Molecular Sciences, Instituto Superior Técnico, Universidade de Lisboa, Av. Rovisco Pais, 1049-001 Lisboa, Portugal. E-mail: anuppaul@tecnico.ulisboa.pt, pombeiro@tecnico.ulisboa.pt*

[b] *Center of Physics and Engineering of Advanced Materials, Laboratory for Physics of Materials and Emerging Technologies, Instituto Superior Técnico, Universidade de Lisboa, 1049-001 Lisboa, Portugal. E-mail: biljana.paunkovic@tecnico.ulisboa.pt*

[c] *Department of Chemistry, Faculty of Science, Helwan University, Ain Helwan, Cairo 11795, Egypt*

[d] *Vinča Institute of Nuclear Sciences-National Institute of the Republic of Serbia, University of Belgrade, Mike Petrovića Alasa 12-14, 11000 Belgrade, Serbia*

[e] *Department of Chemistry, King Saud University, Riyadh-11451, Kingdom of Saudi Arabia*

[f] *Departamento de Engenharia Química, Instituto Superior Técnico, Universidadede Lisboa, Lisbon, Portugal*

† Electronic supplementary information (ESI) available: Experimental details, Scheme S1, Fig. S1–S12 containing ATR-IR, ^1H, ^{13}C- NMR, SXRD, topological, EIS, Nyquist plots, XPS, SEM and stability tests of **Co-CP**, **Ni-CP** and **CoNi-CP**. Tables S1–S3 present the single crystal XRD data of the crystal structures **Co-CP** and **Ni-CP**. Table S4 presents the EDX data of **CoNi-CP** and Table S5 contains OER comparison parameters. CCDC 2308477 and 2308478. For ESI and crystallographic data in CIF or other electronic format see DOI: **https//doi.org/10.1039/d4ce00179f**

Nonetheless, with a few notable exceptions, pristine MOFs and CPs' low conductivity is an intrinsic drawback.[8,9,12] Consequently, only a limited number of these materials have been utilized as effective OER electrocatalysts.[8,9,12] Researchers have turned to MOF- and CP-derived materials, synthesized *via* high-temperature pyrolysis, as potential heterogeneous catalysts for the OER.[8,9] However, this pyrolysis process can compromise the parent materials' intrinsic active sites and ordered structure, ultimately diminishing the catalytic activity. Strategies involving architectural modifications of MOFs and CPs have been explored to address these challenges. These modifications include introducing secondary transition metal ions and functionalized conductive linkers, among other innovative approaches.[8,11,13–19] Bimetallic MOFs/CPs in particular have been shown to exhibit better electrocatalytic performance than their monometallic counterparts because of the combined influence of various metals working together and the ability to adjust the engineering of the metal clusters.[6,20,21] Considering catalytic water splitting, heterobimetallic MOFs based on Ni–Fe,[22,23] Ni–Co[24] and Fe–Co[25,26] exhibited an improved electrocatalytic activity towards the OER when compared to monometallic MOFs. For example, nanosheets based on bimetallic Ni–Co MOFs, synthesized from mixed solutions of Ni^{2+}, Co^{2+} and benzenedicarboxylic acid, were reported as efficient electrocatalysts for the OER in alkaline conditions on account of a synergistic effect between the Ni(II) and Co(II) centers.[27] Other heterobimetallic CPs of Co and Ni are known,[6,7,21–23] but there remains a significant untapped potential.

In recent years, amide-functionalized ligands have ushered in a new era of CP innovation.[28] These ligands offer unique binding possibilities with metal ions, leading to the assembly of diverse architectures.[28] In a prior study, we reported several CPs derived from amide-functionalized ligands that exhibited remarkable activity in C–C coupling reactions, dye adsorption, supercapacitors and electrocatalysts for the OER and overall water splitting.[29–32] Distinguished by well-defined structures and tunable properties, these materials present a promising avenue to address challenges associated with conventional catalysts. The intricate interplay between metal centers and organic ligands in CPs/MOFs yields tailored active sites that can enhance OER kinetics. Their inherent porosity can further improve their electrochemical accessibility, facilitating efficient charge transfer.

In our previous work, we systematically changed the position of the pyridine nitrogen atom in amide-based ligands, creating CPs capable of catalysis,[29] dye adsorption,[30] water splitting,[31,32] and supercapacitance.[31] The present study presents a novel amide-based multifunctional pro-ligand, 4-(pyrimidin-5-ylcarbamoyl)benzoic acid (**HL**, Scheme 1), with a pyridinium moiety.

Utilizing this pro-ligand, we successfully synthesized two pristine CPs, **Ni-CP** and **Co-CP**, and found their electrocatalytic activities in the OER. Further, we demonstrated that the heterometallic system (**CoNi-CP**), derived from the combination of the parent metal precursors (Co^{II} and Ni^{II}) and the pro-ligand (**HL**), performs as a better OER electrocatalyst than **Ni-CP** and **Co-CP**.

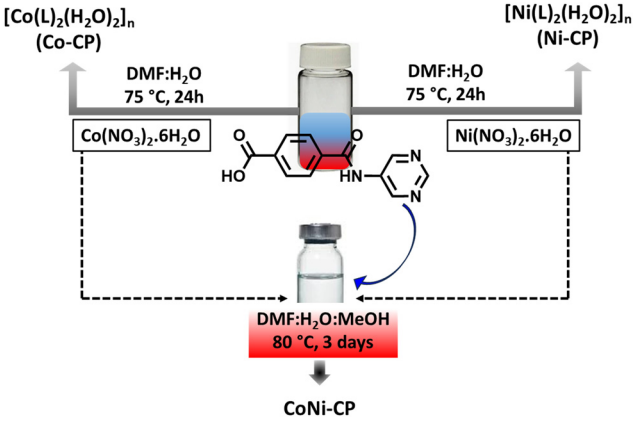

Scheme 1 Synthesis of **Co-NP**, **Ni-CP** and **CoNi-CP**.

Results and discussion

Synthesis and characterization

The synthesis of the pro-ligand, 4-(pyrimidin-5-ylcarbamoyl) benzoic acid (**HL**), followed a multistep process detailed in Scheme S1.† The compound obtained underwent characterization *via* elemental analysis, and IR (Fig. S1†), ^{1}H and ^{13}C-NMR (Fig. S2 and S3†) spectroscopy. CPs **Co-CP** and **Ni-CP** were synthesized by subjecting a DMF solution of **HL** to a hydrothermal reaction in the presence of aqueous solutions of $Co(NO_3)_2{\cdot}6H_2O$ and $Ni(NO_3)_2{\cdot}6H_2O$, respectively, as outlined in Scheme 1. To unravel their structural details, the synthesized CPs were subjected to elemental analysis, IR spectroscopy, and single crystal (SXRD) and powder X-ray diffraction (PXRD) analyses.

The FT-IR spectrum of the pro-ligand **HL** reveals a strong peak at 1705 cm^{-1}, representing the ν(OCO) group's stretching vibrations. Upon binding to the metal centers, this peak shifted noticeably to around 1648 cm^{-1} (Fig. S1†). The ^{1}H NMR spectrum of **HL** reveals distinct resonances arising from the –COO(H) and –N(H) protons, evident at chemical shifts of δ 13.30 and 10.63 ppm, respectively (Fig. S2†). The aromatic protons of the phenyl ring exhibit resonances within the range of δ 8.94–7.44 ppm. In the corresponding ^{13}C NMR spectrum, the signal attributed to the –COOH group is observed at δ 166.25 ppm, accompanied by other resonances at typical positions consistent with the formulation of the compound (Fig. S3†).

To gain insight into the thermal stability of **Co-CP** and **Ni-CP**, a thermogravimetric analysis (TGA) was conducted under a dinitrogen atmosphere, in the temperature range of 30–800 °C at a heating rate of 10 °C per minute, as depicted in Fig. S4.† In the case of **Co-CP** (Fig. S4a†), a weight loss of 6.6% within the temperature range of 150–180 °C corresponds to

the elimination of the coordinated H_2O molecules. This value closely aligns with the calculated value of 6.2%. It displayed stability within the 180–360 °C temperature range, but upon further heating, the polymeric structure ultimately disintegrated.

A similar behavior was observed for **Ni-CP**, as depicted in Fig. S4b:† it exhibited a weight loss of 10.9% in the 150–190 °C range corresponding to the loss of the two coordinated H_2O molecules (calculated value of 11.4%) and showed stability within the temperature range of 190–350 °C beyond which it underwent disintegration.

The surface area and pore characteristics of **Co-CP** and **Ni-CP** were studied by BET N_2 adsorption–desorption analysis, and the isotherm plots are presented in Fig. 1. According to the IUPAC classification, the nitrogen adsorption–desorption isotherm for **Co-CP** closely resembles a type I isotherm (BET surface area of 3 m^2 g^{-1}) (Fig. 1a). The **Ni-CP** exhibited an isotherm reminiscent of a type III one (BET surface area of *ca.* 4 m^2 g^{-1}) (Fig. 1b). To inspect the pore size distribution, non-local density functional theory (NLDFT) analysis was employed, revealing the existence of micropores with diameters in the range of 1–1.5 nm in **Co-CP** (Fig. 1a) and both micropores and mesopores with diameters ranging from 1 to 2.5 nm in **Ni-CP** (inset, Fig. 1b). Furthermore, the N_2 adsorption isotherm of **CoNi-CP** exhibits characteristics typical of a type II isotherm, accompanied by an H2-type hysteresis loop as depicted in Fig. 1c. The BET surface area was found to be 16 m^2 g^{-1} and its pore size distribution revealed the presence of mesopores with diameters ranging from 3 to 11 nanometers (inset, Fig. 1c).

X-ray photoelectron spectroscopy (XPS) was employed to analyze the materials' composition and oxidation states (Fig. 2 and 3). The survey spectra of **Co-CP** and **Ni-CP** revealed the presence of carbon (C), nitrogen (N), oxygen (O) along with Co in **Co-CP** and Ni in **Ni-CP** (Fig. 2). Further, the Co 2p spectrum was analyzed and deconvoluted into two primary components for **Co-CP**. The 780.4 eV and 785.7 eV peaks were assigned to Co^{3+} and Co^{2+} states, respectively (Fig. 3a). Notably, the peak originating from the Co $2p_{1/2}$ part of the doublet was extremely weak, almost indistinguishable

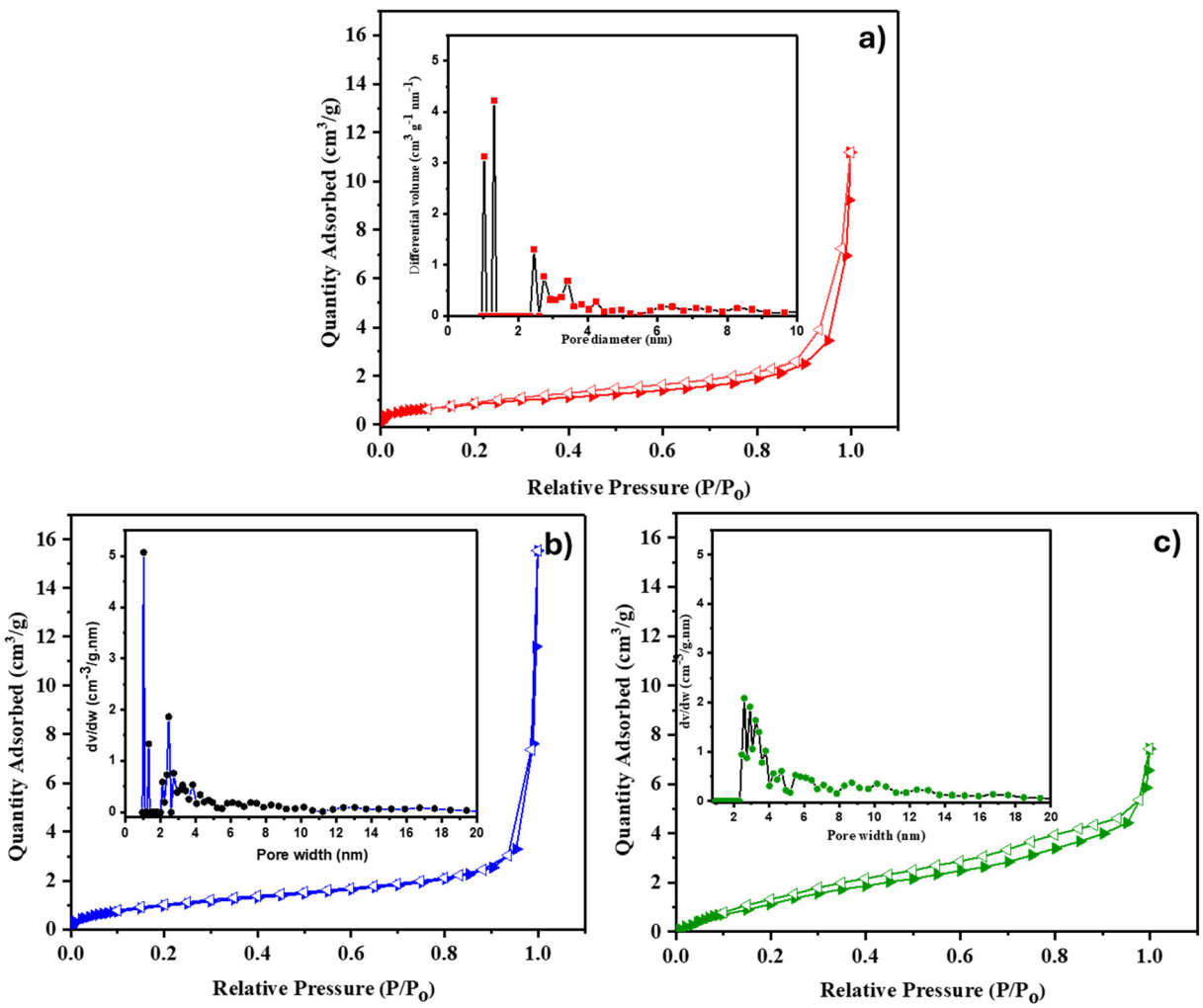

Fig. 1 N_2 adsorption–desorption isotherms at 77 K for **Co-CP** (a), **Ni-CP** (b) and **CoNi-CP** (c). Inset: Non-local density functional theory (NLDFT) pore size distribution. Filled arrows indicate adsorption and hollow arrows indicate desorption.

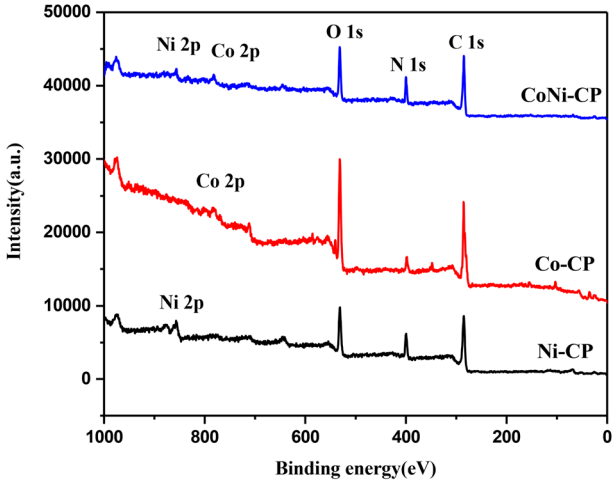

Fig. 2 XPS survey spectra for **Co-CP**, **Ni-CP** and **CoNi-CP**.

from the background noise, and therefore not presented. The Ni 2p spectrum for **Ni-CP** displayed a distinctive doublet structure consisting of Ni $2p_{1/2}$ and Ni $2p_{3/2}$, each further deconvoluted into three components (Fig. 3b). The peaks at 855.9 eV and 873.6 eV were attributed to Ni^{2+}, while those at 860.4 eV and 877.4 eV corresponded to Ni^{3+}. Additionally, two other peaks were identified as satellite features. XPS analysis of **CoNi-CP** is discussed below.

Atomic percentages of elements derived from the survey spectra are shown in Table 1. A low atomic percentage below 1% for Ni and Co is observed in all the samples. **Co-CP** is more oxidized than the other two samples with a correspondingly lower amount of N. The amount of C is constant in all samples.

SEM analysis of the CPs (**Co-CP** and **Ni-CP**) shows a polyhedral morphology composed of multiple stacking sheets (Fig. 4). Furthermore, EDX analysis was conducted to complement our findings. EDX allowed us to quantitatively determine the elemental composition of CPs **Co-CP** and **Ni-CP**, confirming the presence of C, N, oxygen O, and cobalt (Co) for **Co-CP**, and nickel (Ni) for **Ni-CP** (Fig. S5†).

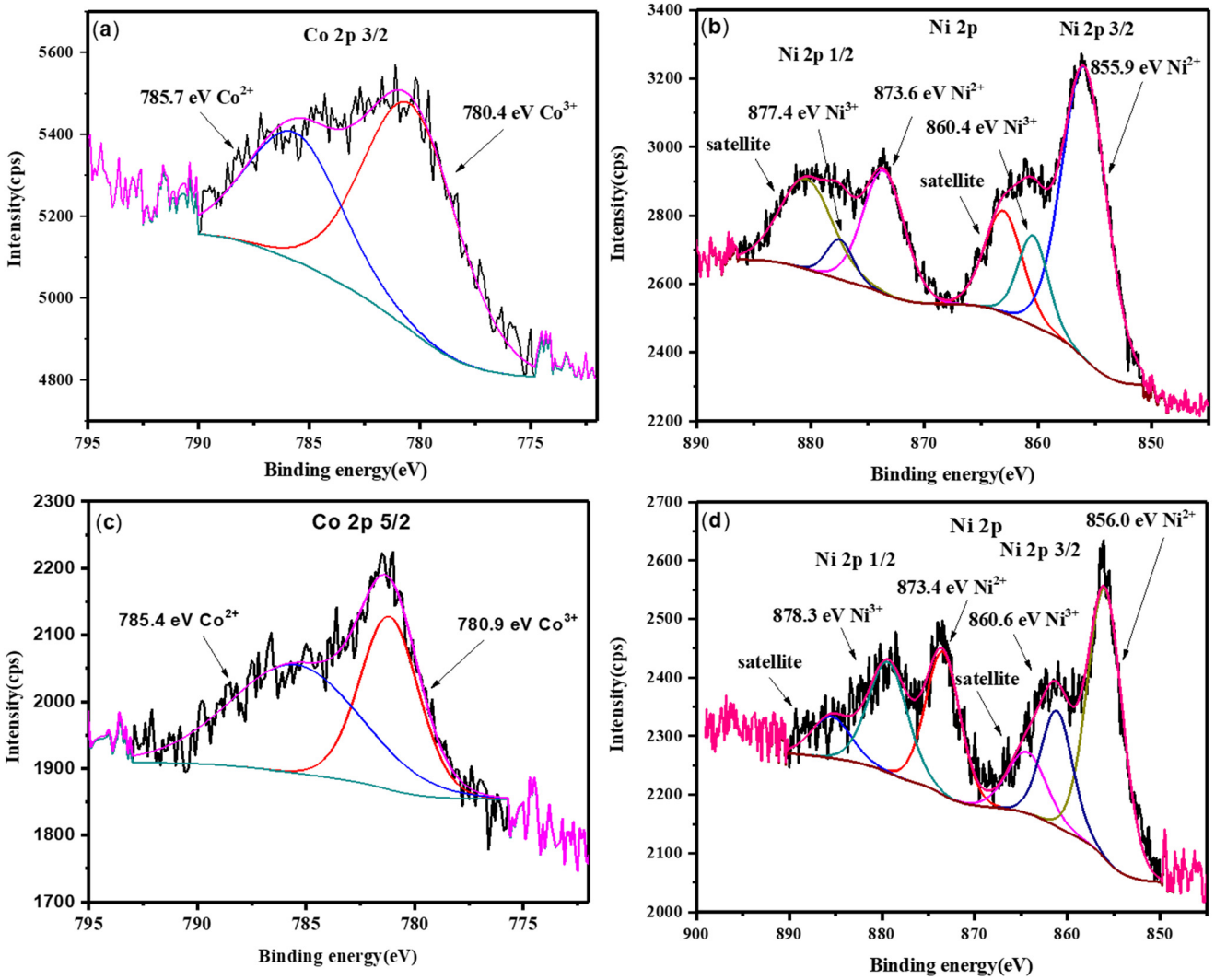

Fig. 3 High resolution XPS spectra: (a) Co 2p for **Co-CP**; (b) Ni 2p for **Ni-CP**; (c) Co 2p for **CoNi-CP** and (d) Ni 2p for **CoNi-CP**.

Table 1 Atomic percentages of elements in samples as derived by XPS

	Ni	Co	C	O	N
Co-CP		0.4%	67.3%	27.7%	4.6%
Ni-CP	0.9%		67.0%	18.5%	13.6%
CoNi-CP	0.3%	0.5%	65.8%	19.8%	13.6%

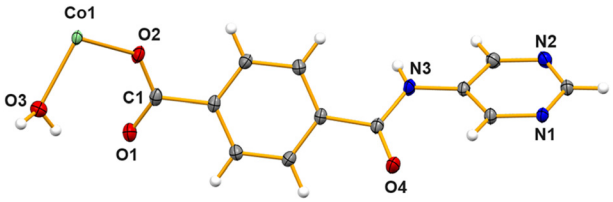

Fig. 5 The ORTEP representation (drawn at 30% probability level) of the asymmetric unit of $[Co^{II}(L)_2(H_2O)_2]_n$ (**Co-CP**) with a partial atom labelling scheme, shown as a representative for **Co-CP** and **Ni-CP**.

X-ray crystallography

Polymers $[Co^{II}(L)_2(H_2O)_2]_n$ (**Co-CP**) and $[Ni^{II}(L)_2(H_2O)_2]_n$ (**Ni-CP**) are isomorphous and isostructural, with their asymmetric units containing one metal cation (Co^{II} in **Co-CP** or Ni^{II} in **Ni-CP**), a pyrimidine–carboxylate ligand (L) and a coordinated water molecule (Fig. 5 for **Co-CP**). Symmetry expansion uncovers the metals in nearly perfect octahedral geometries constructed from four L^- moieties acting as $\kappa N_{pyrimidine}$-$O_{carboxylate}$ bridging ligands in the equatorial positions and two water molecules in the axial sites thus leading to N–**M**–N and $O_{carboxylate}$–**M**–$O_{carboxylate}$ angles of 180° and the O_{water}–**M**–N ones (values between 85.96(5) to 94.04(5)°, Table S2†). Despite having comparable covalent radii, the M–O_{water}, M–$O_{carboxylate}$ and M–$N_{pyrimidine}$ bond distances are slightly different. The aromatic phenyl and pyrimidine rings are

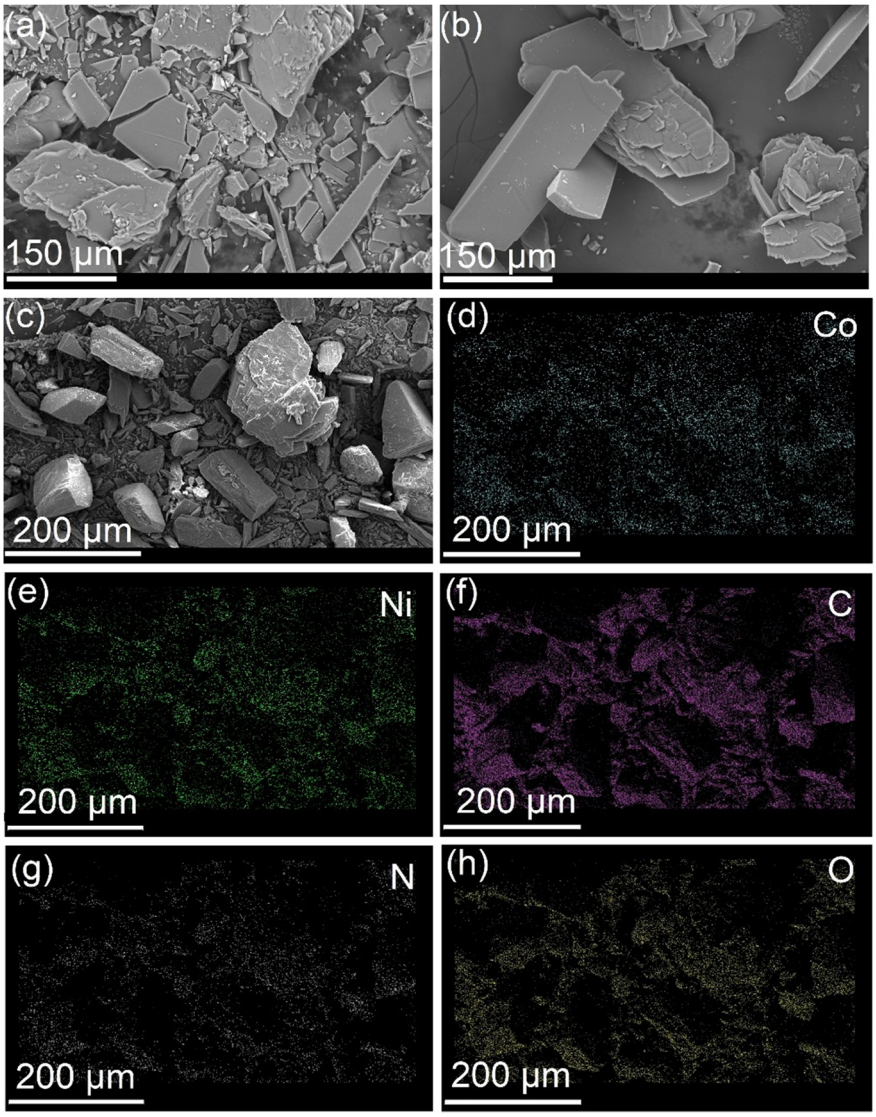

Fig. 4 SEM images of **Co-CP** (a), **Ni-CP** (b), **CoNi-CP** (c) and the corresponding elemental mapping of **CoNi-CP** using EDS: Co (d), Ni (e), C (f), N (g) and O (h).

similarly twisted (dihedral angles of the corresponding least square planes: 60.52° in **Co-CP** and 61.28° in **Ni-CP**).

Both polymers form elongated M_2L_2 metallacycles (Fig. 6) assuming intermetallic distances of 13.470 (**Co-CP**) and 13.435 Å (**Ni-CP**) in loop-chain like one-dimensional network with base vector: [1$\bar{0}$1] (Fig. S6†).

Water ligands and the NH amide donors allow the formation of several H-bonding interactions in both CPs, which ultimately expand their 1D structures to the third dimension. The first level of such contacts in **Co-CP** is exemplified in Fig. S7a† and results from patterns between the N_{amide} and the $O_{carboxylate}$ and the O_{water} and the O_{amide}; water molecules and pyrimidine describe a relation. In **Ni-CP**, the interaction between O_{water} and the O_{amide} was not detected, but the others described for **Co-CP** are active and shown in Fig. S7b.† Intramolecular interactions are common to both polymers. The highest second-level descriptors in **Co-CP** involve the O_{water} and the O_{amide}, or the $N_{pyrimidine}$ atoms (see Fig. S7a†). In **Ni-CP**, however, that category involves contacts engaging the N_{amide} and the $O_{carboxylate}$, as well as the O_{water} and the $N_{pyrimidine}$. It is worth mentioning that H-bonds of such types are common in urea- and amide-based MOF systems.[33,34] The resulting three-dimensional supramolecular architecture is exemplified in Fig. 7 for the polymer **Co-CP**.

To enhance our comprehension of the crystal structures of **Co-CP** and **Ni-CP**, we delved into their topological characteristics by simplifying their complex multidimensional arrangements into more manageable node-and-linker networks. The topological analysis unveiled the similarity in the framework architectures of both structures and identical 2,4-connected binodal networks (Fig. 8). However, when combining the 2D CPs and their hydrogen-bonding interactions, we notice a 3,5,6 trinodal net in **Co-CP** (Fig. S8a†) and a 2,4,6 connected trinodal net in **Ni-CP** (Fig. S8b†).

We also conducted powder X-ray diffraction (PXRD) analyses of **Co-CP**, **Ni-CP** and **CoNi-CP**, which illustrate the similarity of the synthesized bulk materials (Fig. 9).

Electrocatalytic studies

The synthesized CPs **Co-CP** and **Ni-CP** were evaluated as electrocatalysts for the OER. Linear sweep voltammograms of

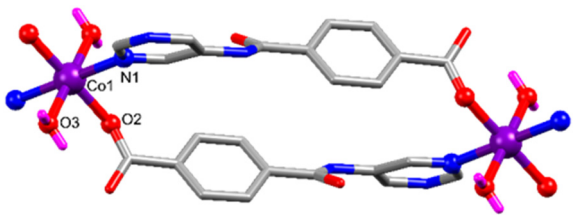

Fig. 6 The elongated M_2L_2 metallacycle in $[Co(L)_2(H_2O)_2]_n$ (**Co-CP**), shown as a representative for **Co-CP** and **Ni-CP**. H-atoms are omitted for clarity, except those of water ligands.

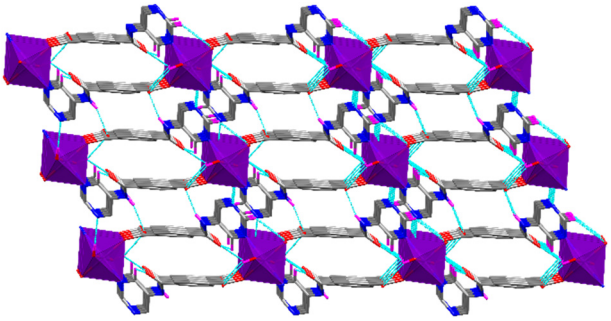

Fig. 7 H-bonds supported three dimensional architectures in **Co-CP**. All H-atoms except those that participate in H-bonds are omitted for clarity, and the metal environments are presented in polyhedra.

these materials were recorded under OER polarization conditions and compared to IrO_2, a benchmark catalyst for this reaction, as illustrated in Fig. 10. Both CPs exhibited nearly identical, yet superior, catalytic activity compared to the benchmark IrO_2 catalyst.

The catalytic performance of these materials was evaluated based on several key parameters, including the onset potential (E_{onset}), the overpotential required to achieve a current density of 10 mA cm^{-2} (η_{10}), the current at an overpotential of 500 mV (j_{500}), and the Tafel slope. Both CPs displayed excellent OER activity in 1 M KOH solution, with **Ni-CP** exhibiting slightly higher performance than **Co-CP**, possibly due to the mesoporous structure enabling easier transfer of reactant/products to/from the active sites. Tafel analysis revealed a somewhat lower Tafel slope value for **Ni-CP** (110 mV dec^{-1}) than for **Co-CP** (120 mV dec^{-1}). **Ni-CP** also displayed a lower E_{onset} (1.549 V) and η_{10} (396 mV) compared to **Co-CP** (E_{onset} = 1.564 V, η_{10} = 422 mV).

Double-layer capacitance (C_{dl}) measurements were also performed in a non-faradaic region of 125 mV around the open circuit potential, as shown in Fig. S9.† The two CPs presented similar C_{dl} values (**Co-CP**: 0.380 mF cm^{-2}; and **Ni-CP**: 0.299 mF cm^{-2}) suggesting a similar electrochemically active surface area (ECSA). Additionally, EIS measurements were conducted for both materials under OER polarization conditions (Fig. S10†), allowing the determination of both the electrolyte resistance (R_s) and the charge-transfer resistance (R_{ct}). R_s showed similar values for both the CPs, with slight variations due to differences in cell geometry. In contrast, R_{ct}, equivalent to the semicircle diameter observed in the Nyquist plots, exhibited a lower value of 10 Ω for **Co-CP** compared to 76 Ω for **Ni-CP**.

Motivated by the high performance of the CPs **Co-CP** and **Ni-CP**, we synthesized a heterobimetallic CP using the same

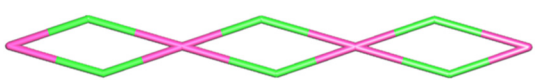

Fig. 8 Node-and-linker-type description of the 2D coordination frameworks in **Co-CP** and **Ni-CP** (metal centres indicated as pink and ligands in green).

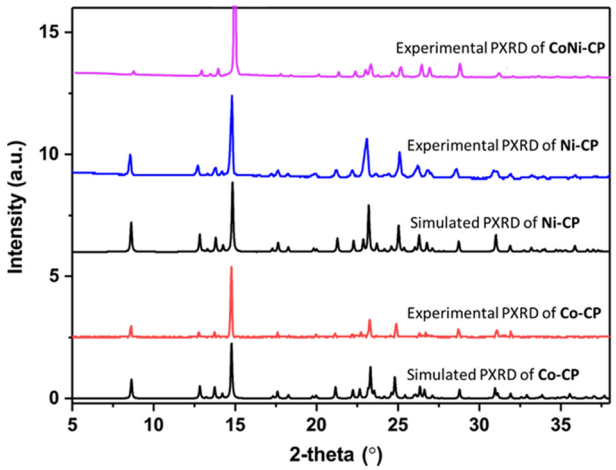

Fig. 9 PXRD data of **Co-CP**, **Ni-CP** and **CoNi-CP**.

set of starting compounds. One of the key driving factors behind the synthesis of the heterobimetallic CPs is the potential for synergy between the two different metals. The successful synthesis of **CoNi-CP** was achieved through the combination of equimolar amounts of $Co(NO_3)_2{\cdot}6H_2O$ and $Ni(NO_3)_2{\cdot}6H_2O$ with the organic linker **HL** during a hydrothermal process (as outlined in Scheme 1), and it represents a pivotal step in our research endeavor. The characterization studies conducted on **CoNi-CP** offer valuable insights into the composition and distribution of Ni and Co metals within this bimetallic CP. Inductively coupled plasma (ICP) analysis was employed to determine the global concentration of metal centers in the synthesized pink crystalline material, and the Ni to Co ratio of 1 : 1 was obtained. Similar PXRD patterns were observed for **CoNi-CP** to those of **Co-CP** and **Ni-CP** (Fig. 9). Moreover, the SEM images illustrate that the block morphology of **CoNi-CP** (Fig. 4c) closely resembles that of the monometallic CPs, **Co-CP** and **Ni-CP** (Fig. 4a and b). Furthermore, EDS mapping offers valuable insights into the distribution of Ni and Co metal centers. The co-localization of Ni and Co metal centers and their even distribution across the crystal surface provide further evidence of the homogeneous integration of these metals within the same material (Fig. 4d–h and Table S4†).

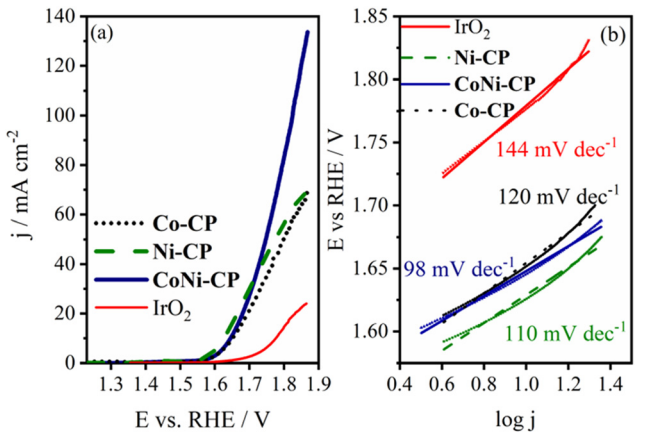

Fig. 10 OER LSV curves of **Co-CP**, **Ni-CP** and **CoNi-CP** in 1 M KOH electrolyte (a), and the corresponding Tafel plots and Tafel slope values (b).

The elemental composition was further determined by XPS analysis (Fig. 3c and d). It confirms the presence of Ni, Co, O, N and C in the samples as expected. High resolution spectra of C 1s, O 1s and N 1s for **CoNi-CP** are shown in Fig. S11.† The spectrum for C 1s is deconvoluted into four components (Fig. S11a†). Peaks at 281.7, 284.1, 285.2 and 286.5 eV can be identified as carbon originating from the C–metal (Co, Ni) bond, pyrimidine, amide and carboxylate structures, respectively.[35–37] The spectrum of O 1s can be fitted with five components (Fig. S11b†). The peak at 527.5 eV can be assigned to the M–O bond (M = Co or Ni). Three peaks at 528.8, 530.8 and 532.1 eV belonging to pyrimidine, amide and carboxylate groups, respectively, are the same as for C 1s confirming the presence of these structures. Furthermore, an additional peak at 533.7 eV is attributed to the presence of adsorbed water oxygen molecules in the structure.[37,38] The spectrum for N 1s (Fig. S11c†) shows only two components, which originate from pyrimidine (398.9 eV) and amide (400.2 eV) structures.[35–38] Moreover, Co 2p and Ni 2p spectra for **CoNi-CP** (Fig. 3c and d) are deconvoluted analogously to the spectra of CPs **Co-CP** and **Ni-CP** with only slight differences in peak positions.[39,40] They confirm the presence of the same components as those of CPs **Co-CP** and **Ni-CP**.

The OER activity of **CoNi-CP** was studied under the same experimental conditions as in the case of its monometallic counterparts. It showed an excellent catalytic activity, surpassing the performance of the individual pristine CPs **Co-CP** and **Ni-CP** as well as of the benchmark IrO_2, with a current density of 134 mA cm^{-2} at a potential of 1.87 V *vs.* RHE (value *ca.* 2× and 5.4× higher than that for monometallic CPs and for commercial IrO_2, respectively, Fig. 10a). Tafel analysis revealed a Tafel slope value for **CoNi-CP** of 98 mV dec^{-1} that is *ca.* 46 mV dec^{-1} lower than that of IrO_2. E_{onset} and η_{10} were determined to be 1.557 V and 416 mV (*ca.* 120 mV lower compared to IrO_2), respectively. The difference between the bi- and monometallic CPs is further expressed in the current density at an overpotential of 500 mV, with **CoNi-CP** reaching 40.8 mA cm^{-2} compared with 29.7 and 38.3 mA cm^{-2} reached by CPs **Co-CP** and **Ni-CP**, respectively. The double-layer capacitance for the studied material was determined to be 1.33 mF cm^{-2}, *i.e.*, one order of magnitude higher compared to **Co-CP** and **Ni-CP**, Fig. S9.† This indicates that the ECSA of **CoNi-CP** is significantly higher than those of the monometallic CPs, justifying the higher activity observed at more positive OER potentials.

The assessment of R_s and R_{ct} from the Nyquist plot (Fig. S10†), reveals the R_{ct} value for the bimetallic **CoNi-CP** of 35 Ω. The R_{ct} value of 35 Ω for the bimetallic **CoNi-CP** falls between the values of **Co-CP** and **Ni-CP** indicating a moderate charge-transfer resistance.

Investigation of the durability of the three CPs over 10 hours further supports the superior performance of the

bimetallic **CoNi-CP**, Fig. S12.† An initial drop of the current density was observed in the case of all three CPs. However, the OER current densities recorded using the monometallic CPs fall close to zero by the end of the 10 hour study. Conversely, current densities recorded using the bimetallic CP stabilize and remain unchanged after 5 h. The superior electrocatalytic performance of the bimetallic **CoNi-CP** for the OER compared to the monometallic CPs (**Co-CP** and **Ni-CP**) may be attributed to a synergistic effect in the heterobimetallic materials.[27] A **CoNi-CP** working electrode was additionally analysed before and after the electrochemical tests by using SEM analysis with elemental mapping, depicted in Fig. S12.† The analysis revealed minor alterations in the electrode's morphology and the distribution of elements, without notable formation of oxides or oxyhydroxides, suggesting that the bimetallic **CoNi-CP** functions as hybrids combining attributes of both molecular and heterogeneous electrocatalysts, showcasing distinctive metal active sites.

We have also compared the electrocatalytic performance of our materials towards the OER with those of other MOFs in recent advancements in the field. For example, Bridha *et al.* introduced 2D MOFs with redox-active metal centers, Ni(II), Co(II) and Cu(II), paired with electron-rich linkers.[41] These MOFs displayed promising OER activity, with overpotentials in the range of 370–430 mV range comparable to ours, and Tafel slope values of 100–130 mV dec^{-1} that are higher than (hence, not so favourable as) ours. In another study, Li *et al.* synthesized 2D CPs with Co(II) and Ni(II) centers using 3,5-(di(2′,5′-dicarboxylphenyl)benozoic acid as the ligand source, showing overpotentials of 395 mV and 475 mV, with corresponding Tafel slopes of 68 and 143 mV dec^{-1}.[42] Recently, Koner *et al.*[15] explored the role of mesaconate coordination in the OER with their Ni(II)-based CPs. $[Ni(MCA)(bipy)(H_2O)_2]_n$ required 530 mV to reach a current density of 10 mA cm^{-2}, while another CP without mesaconate exhibited an even higher overpotential of 630 mV. The Tafel slope values were 90 and 137 mV dec^{-1}, respectively. This comparative analysis highlights the comparable or superior activity of our CPs towards the OER, emphasizing their potential in advancing electrocatalytic applications. Further comparison with other relevant CoNi CPs (Table S5†) shows that our catalysts do not always exhibit a more favourable overpotential and Tafel slope, but it is noteworthy that such CPs, in contrast to ours, are mostly non-pristine.

Conclusions

In this study, we have successfully synthesized and characterized two monometallic coordination polymers (CPs), **Co-CP** and **Ni-CP**, as well as a heterobimetallic CP, **CoNi-CP**, using a novel amide-based multifunctional proligand (**HL**) and assessed their electrocatalytic performance for the OER. The **Co-CP** and **Ni-CP** crystal structures were found to be isomorphous and isostructural, with octahedral metal coordination geometries and the formation of elongated M_2L_2 metallacycles. The 1D network structures were expanded into three dimensions through hydrogen-bonding interactions, resulting in unique supramolecular architectures. A topological analysis revealed the underlying framework architectures, which were characterized by 2,4-connected binodal networks in both structures.

Our findings demonstrate the promising electrocatalytic activity of these CPs, with **CoNi-CP**, in particular, outperforming both its monometallic counterparts and the benchmark catalyst, IrO_2, with a low Tafel slope of 98 mV dec^{-1} (*ca.* 46 mV dec^{-1} lower than that of commercial IrO_2), an overpotential of 416 mV at 10 mA cm^{-2} (*ca.* 120 mV lower than that of IrO_2), and current density of 40.8 mA cm^{-2} at 500 mV overpotential (*ca.* 5x higher than that of IrO_2), indicating it as one of the best-performing electrocatalysts for the OER. This heterobimetallic CP (**CoNi-CP**) not only exhibited an enhanced OER activity (due to improved electrochemically active surface area and lower charge transfer resistance), but also a higher long-term durability, making it a highly promising electrocatalyst. Our results also suggest the occurrence of a synergistic effect of the Co(II) and Ni(II) metals. Overall, this study provides valuable insights into the design and development of highly efficient electrocatalysts for the oxygen evolution reaction.

Conflicts of interest

There are no conflicts to declare.

Acknowledgements

A. P., S. H. and B. Š. are grateful to the Fundação para a Ciência e a Tecnologia (FCT), and IST ID, Portugal, for financial support through "DL/57/2017" (contract no. IST-ID/197/2019, DOI: **https://doi.org/10.54499/DL57/2016/CP1384/CT0081** and IST-ID/156/2018). This work has also been partially supported by the FCT through projects UIDB/00100/2020, UIDP/00100/2020, and LA/P/0056/2020 of Centro de Química Estrutural. R. A. K. gratefully acknowledges the Researchers Supporting Project (Project number, RSP2024R400). The authors also acknowledge the Portuguese NMR Network (IST-UL Centre) for access to the NMR facility.

References

1 S. Lee, J. Choi, M. Kim, J. Park, M. Park and J. Cho, Material Design and Surface Chemistry for Advanced Rechargeable Zinc-Air Batteries, *Chem. Sci.*, 2022, **13**, 6159–6180, DOI: **10.1039/d1sc07212a**.

2 Y. Cheng, Y. Wang, Q. Wang, Z. Liao, N. Zhang, Y. Guo and Z. Xiang, Hierarchically Porous Metal-Free Carbon with Record High Mass Activity for Oxygen Reduction and Zn-Air Batteries, *J. Mater. Chem. A*, 2019, **7**, 9831–9836.

3 A. K. Thakur, M. Majumder, S. P. Patole, K. Zaghib and M. V. Reddy, Metal-Organic Framework-Based Materials: Advances,

Exploits, and Challenges in Promoting Post Li-Ion Battery Technologies, *Mater. Adv.*, 2021, **2**, 2457–2482.

4 C. Li, Y. Gao, X. Xia, J. Zhu, X. Wang and Y. Fu, Hierarchically Structured Two-Dimensional Bimetallic CoNi-Hexaaminobenzene Coordination Polymers Derived from Co(OH)2 for Enhanced Oxygen Evolution Catalysis, *Small*, 2020, **16**(8), 1907043.

5 Y. Lee, J. Suntivich, K. J. May, E. E. Perry and Y. Shao-Horn, Synthesis and Activities of Rutile IrO2 and RuO2 Nanoparticles for Oxygen Evolution in Acid and Alkaline Solutions, *J. Phys. Chem. Lett.*, 2012, **3**(3), 399–404.

6 S. Li, Y. Gao, N. Li, L. Ge, X. Bu and P. Feng, Transition Metal-Based Bimetallic MOFs and MOF-Derived Catalysts for Electrochemical Oxygen Evolution Reaction, *Energy Environ. Sci.*, 2021, **14**, 1897–1927.

7 J. Jiang, X. L. Zhou, H. G. Lv, H. Q. Yu and Y. Yu, Bimetallic-Based Electrocatalysts for Oxygen Evolution Reaction, *Adv. Funct. Mater.*, 2023, **33**, 2212160.

8 Q. Liang, J. Chen, F. Wang and Y. Li, Transition Metal-Based Metal-Organic Frameworks for Oxygen Evolution Reaction, *Coord. Chem. Rev.*, 2020, **424**, 213488.

9 Y. Mousazade, M. R. Mohammadi, P. Chernev, R. Bagheri, Z. Song, H. Dau and M. M. Najafpour, Revisiting Metal-Organic Frameworks for Oxygen Evolution: A Case Study, *Inorg. Chem.*, 2020, **59**(20), 15335–15342.

10 S. Lyu, C. Guo, J. Wang, Z. Li, B. Yang, L. Lei, L. Wang, J. Xiao, T. Zhang and Y. Hou, Exceptional Catalytic Activity of Oxygen Evolution Reaction via Two-Dimensional Graphene Multilayer Confined Metal-Organic Frameworks, *Nat. Commun.*, 2022, **13**(1), 6171, DOI: **10.1038/s41467-022-33847-z**.

11 C. Li, H. Zhang, M. Liu, F.-F. Lang, J. Pang and X.-H. Bu, Recent Progress in Metal–Organic Frameworks (MOFs) for Electrocatalysis, *Ind. Chem. Mater.*, 2023, **1**, 9–38.

12 Q. Zhao, D. Zhu, X. Zhou, S. H. Li, X. Sun, J. Cui, Z. Fan, M. Guo, J. Zhao, B. Teng and B. Cheng, Conductive One-Dimensional Coordination Polymers with Tunable Selectivity for the Oxygen Reduction Reaction, *ACS Appl. Mater. Interfaces*, 2021, **13**(44), 52960–52966.

13 L. Han, S. Dong and E. Wang, Transition-Metal (Co, Ni, and Fe)-Based Electrocatalysts for the Water Oxidation Reaction, *Adv. Mater.*, 2016, **28**, 9266–9291.

14 Z. Q. Jiang, Y. F. Li, X. J. Zhu, J. Lu, L. Zhang and T. Wen, Ni(Ii)-Based Coordination Polymers for Efficient Electrocatalytic Oxygen Evolution Reaction, *RSC Adv.*, 2018, **8**(67), 38562–38565.

15 T. Kumar, A. Karmakar, A. Halder and R. R. Koner, Ni(II)-Based Coordination Polymer with Pi-Conjugated Organic Linker as Catalyst for Oxygen Evolution Reaction Activity, *Energy Fuels*, 2022, **36**, 2722–2730.

16 Y. Zhao, Z. M. Zhai, X. Y. Liu, X. G. Yang, L. F. Ma and L. Y. Wang, Two Cobalt(II) Coordination Polymers Based on 5-i-Butoxyisophthalate and Dipyridyl: Syntheses, Structures and Efficient Oxygen Evolution Reaction, *J. Solid State Chem.*, 2019, **278**, 120913.

17 H. Jia, Y. Yao, J. Zhao, Y. Gao, Z. Luo and P. Du, A Novel Two-Dimensional Nickel Phthalocyanine-Based Metal-Organic Framework for Highly Efficient Water Oxidation Catalysis, *J. Mater. Chem. A*, 2018, **6**(3), 1188–1195.

18 S. K. Konavarapu, D. Ghosh, A. Dey, D. Pradhan and K. Biradha, Isostructural NiII Metal–Organic Frameworks (MOFs) for Efficient Electrocatalysis of Oxygen Evolution Reaction and for Gas Sorption Properties, *Chem. – Eur. J.*, 2019, **25**, 11141–11146.

19 C. Chen, J. Li, Z. Lv, M. Wang and J. Dang, Recent Strategies to Improve the Catalytic Activity of Pristine MOFs and Their Derived Catalysts in Electrochemical Water Splitting, *Int. J. Hydrogen Energy*, 2023, **48**, 30435–30463.

20 N. Raza, T. Kumar, V. Singh and K. H. Kim, Recent Advances in Bimetallic Metal-Organic Framework as a Potential Candidate for Supercapacitor Electrode Material, *Coord. Chem. Rev.*, 2021, **430**, 213660.

21 S. Sanati, R. Abazari, J. Albero, A. Morsali, H. García, Z. Liang and R. Zou, Metal–Organic Framework Derived Bimetallic Materials for Electrochemical Energy Storage, *Angew. Chem.*, 2021, **60**, 11048–11067.

22 D. Senthil Raja, X. F. Chuah and S. Y. Lu, In Situ Grown Bimetallic MOF-Based Composite as Highly Efficient Bifunctional Electrocatalyst for Overall Water Splitting with Ultrastability at High Current Densities, *Adv. Energy Mater.*, 2018, **8**(23), 201801065.

23 F. Zheng, Z. Zhang, D. Xiang, P. Li, C. Du, Z. Zhuang, X. Li and W. Chen, Fe/Ni Bimetal Organic Framework as Efficient Oxygen Evolution Catalyst with Low Overpotential, *J. Colloid Interface Sci.*, 2019, **555**, 541–547.

24 W. Zhou, D. Huang, Y. Wu, J. Zhao, T. Wu, J. Zhang, D. Li, C. Sun, P. Feng and X. Bu, Stable Hierarchical Bimetal–Organic Nanostructures as HighPerformance Electrocatalysts for the Oxygen Evolution Reaction, *Angew. Chem., Int. Ed.*, 2019, **58**, 4227–4231.

25 X. Fang, L. Jiao, S. H. Yu and H. L. Jiang, Metal–Organic Framework-Derived FeCo-N-Doped Hollow Porous Carbon Nanocubes for Electrocatalysis in Acidic and Alkaline Media, *ChemSusChem*, 2017, **10**(15), 3019–3024.

26 L. Yang, S. Feng, G. Xu, B. Wei and L. Zhang, Electrospun MOF-Based FeCo Nanoparticles Embedded in Nitrogen-Doped Mesoporous Carbon Nanofibers as an Efficient Bifunctional Catalyst for Oxygen Reduction and Oxygen Evolution Reactions in Zinc-Air Batteries, *ACS Sustainable Chem. Eng.*, 2019, **7**(5), 5462–5475.

27 S. Zhao, Y. Wang, J. Dong, C. T. He, H. Yin, P. An, K. Zhao, X. Zhang, C. Gao, L. Zhang, J. Lv, J. Wang, J. Zhang, A. M. Khattak, N. A. Khan, Z. Wei, J. Zhang, S. Liu, H. Zhao and Z. Tang, Ultrathin Metal-Organic Framework Nanosheets for Electrocatalytic Oxygen Evolution, *Nat. Energy*, 2016, **1**(12), 16184.

28 A. Karmakar and A. J. L. Pombeiro, Recent Advances in Amide Functionalized Metal Organic Frameworks for Heterogeneous Catalytic Applications, *Coord. Chem. Rev.*, 2019, **395**, 86–129.

29 A. Paul, L. M. D. R. S. Martins, A. Karmakar, M. L. Kuznetsov, A. S. Novikov, M. F. C. Guedes da Silva and A. J. L. Pombeiro, Environmentally Benign Benzyl Alcohol

Oxidation and C-C Coupling Catalysed by Amide Functionalized 3D Co(II) and Zn(II) Metal Organic Frameworks, *J. Catal.*, 2020, **385**, 324–337.

30 A. Paul, K. Das, A. Karmakar, M. F. C. Guedes Da Silva and A. J. L. Pombeiro, A Mechanistic Insight into the Rapid and Selective Removal of Congo Red by an Amide Functionalised Zn(Ii) Coordination Polymer, *Dalton Trans.*, 2020, **49**(37), 12970–12984.

31 A. Paul, K. K. Upadhyay, G. Backović, A. Karmakar, L. F. Vieira Ferreira, B. Šljukić, M. F. Montemor, M. F. C. Guedes Da Silva and A. J. L. Pombeiro, Versatility of Amide-Functionalized Co(II) and Ni(II) Coordination Polymers: From Thermochromic-Triggered Structural Transformations to Supercapacitors and Electrocatalysts for Water Splitting, *Inorg. Chem.*, 2020, **59**(22), 16301–16318.

32 A. Paul, K. Radinović, S. Hazra, D. Mladenović, B. Šljukić, R. A. Khan, M. F. C. Guedes da Silva and A. J. L. Pombeiro, Electrocatalytic Behavior of an Amide Functionalized Mn(II) Coordination Polymer on ORR, OER and HER, *Molecules*, 2022, **27**(21), 7323.

33 A. Karmakar, S. Hazra and A. J. L. Pombeiro, Urea and Thiourea Based Coordination Polymers and Metal-Organic Frameworks: Synthesis, Structure and Applications, *Coord. Chem. Rev.*, 2022, **453**, 214314.

34 C. R. Groom, I. J. Bruno, M. P. Lightfoot and S. C. Ward, The Cambridge Structural Database, *Acta Crystallogr., Sect. B: Struct. Sci., Cryst. Eng. Mater.*, 2016, **72**(2), 171–179.

35 S. Chen, J. Duan, M. Jaroniec and S. Z. Qiao, Three-Dimensional N-Doped Graphene Hydrogel/NiCo Double Hydroxide Electrocatalysts for Highly Efficient Oxygen Evolution, *Angew. Chem., Int. Ed.*, 2013, **52**, 13567–13570.

36 N. A. Elessawy, G. Backović, J. Hirunthanawat, M. Martins, L. Rakočević, M. H. Gouda, A. Toghan, M. E. Youssef, B. Šljukić and D. M. F. Santos, From PET Bottles Waste to N-Doped Graphene as Sustainable Electrocatalyst Support for Direct Liquid Fuel Cells, *Catalysts*, 2023, **13**(3), 525.

37 A. Singh, K. R. Ansari, D. S. Chauhan, M. A. Quraishi and S. Kaya, Anti-Corrosion Investigation of Pyrimidine Derivatives as Green and Sustainable Corrosion Inhibitor for N80 Steel in Highly Corrosive Environment: Experimental and AFM/XPS Study, *Sustainable Chem. Pharm.*, 2020, **16**, 100257.

38 R. K. Mehta, S. K. Gupta and M. Yadav, Studies on Pyrimidine Derivative as Green Corrosion Inhibitor in Acidic Environment: Electrochemical and Computational Approach, *J. Environ. Chem. Eng.*, 2022, **10**(5), 108499.

39 P. Salunkhe and M. Ali, Investigation on tailoring physical properties of Nickel Oxide thin films grown by dc magnetron sputtering, *Mater. Res. Express*, 2020, **7**, 016427.

40 Y. Li, X. Wu, S. Wang, W. Wang, Y. Xiang, C. Dai, Z. Liu, Z. He and X. Wu, Surfactant-Assisted Solvothermal Synthesis of NiCo2O4 as an Anode for Lithium-Ion Batteries, *RSC Adv.*, 2017, **7**(59), 36909–36916.

41 A. Goswami, D. Ghosh, V. V. Chernyshev, A. Dey, D. Pradhan and K. Biradha, 2D-MOFs with Ni(II), Cu(II) and Co(II) as Efficient Oxygen Evolution Electrocatalysts: Rationalization of Catalytic Performance vs Structure of the MOFs and Potential of the Redox Couples, *ACS Appl. Mater. Interfaces*, 2020, **12**(30), 33679–33689.

42 X. K. Wang, J. W. Tian, D. D. Huang, Y. P. Wu, L. Q. Pan and D. S. Li, Two Novel Co(II)/Ni(II) Coordination Polymers Based on 3,5-Di(2′,5′-Dicarboxylphenyl)Benozoic Acid Ligand: Crystal Structures, Magnetic Properties and Oxygen Evolution Reaction, *J. Solid State Chem.*, 2019, **269**, 348–353.

